Applied Energy 339 (2023) 120944

Contents lists available at ScienceDirect

Applied Energy

journal homepage: www.elsevier.com/locate/apenergy

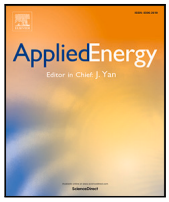

Digital twin of a Fresnel solar collector for solar cooling

Diogo Ortiz Machado [a,b,c], William D. Chicaiza [c], Juan M. Escaño [c], Antonio J. Gallego [c], Gustavo A. de Andrade [b], Julio E. Normey-Rico [b], Carlos Bordons [c,d,*], Eduardo F. Camacho [c,d]

[a] IFRS - Instituto Federal de Educação, Ciencia e Tecnolgia do Rio Grande do Sul, Rua Alfredo Huch, 475, Rio Grande, 96201 460, Rio Grande do Sul, Brazil
[b] UFSC - Universidade Federal de Santa Catarina. Departamento de Automação e Sistemas, R. Eng. Agronômico Andrei Cristian Ferreira, Florianópolis, 88040 900, Santa Catarina, Brazil
[c] US - Universidad de Sevilla. Departamento de Ingeniería de Sistemas y Automática, Camino de los Descubrimientos, Sevilla, 41092, Andalucía, Spain
[d] ENGREEN - Laboratory of Engineering for Energy and Environmental Sustainability, Universidad de Sevilla, Spain

ARTICLE INFO

Dataset link: https://data.mendeley.com/datasets/rzggrvczf6

Keywords:
Adaptive neuro fuzzy inference system
Distributed parameter dynamic model
Dynamic modeling
Validation
Absorption plant

ABSTRACT

This work develops digital entities of a commercial Fresnel Solar Collector (FSC) installed in an absorption cooling plant. The objective is to create and validate models that describe the FSC dynamics across its whole operation range during the day and the night. Thus, the temperatures range between operation temperature of 180 °C and almost ambient temperature due to overnight heat losses. In the same sense, the flow range between zero to 13m^3/h. The idea is that the digital twin will aid start-up and shut-down optimization and control design reliability. The paper employs two modeling approaches, then evaluates their twinning/adaptation time and performance validation. One model uses phenomenological modeling through Partial Differential Equations (PDE) and parameters identification, and another uses a data-driven technique with Adaptive Neuro-Fuzzy Inference Systems (ANFIS). The available measurement data sets comprise 25 days of operation with a sampling time of 20 s which, after outlier removal, filtering and treatment, resulted in 108416 samples. The validation considers six separate operating days. Results show that both models can twinning/adapt considering measured data. The models present pretty good results and are suitable for control and optimization. Besides, this is the first paper considering the FSC mirror defocus action on dynamic modeling and validation.

1. Introduction

The solar power that daily strikes planet earth is the driving energy that sustains all life that evolved to an intricate and delicate equilibrium. Therefore, knowing how to harness this power source in a practical and versatile manner will pave the way for a sustainable future. This work contributes to developing two adaptive models of a Fresnel Solar Collector (FSC) in the framework of digital twins. One uses data-driven neuro-fuzzy (NF) networks, and the other uses phenomenological Partial Differential Equations (PDE) with parameter identification. Both digital entities will plan, integrate, and control the absorption plant installed at the *Escuela Tecnica Superior de Ingenieria* - ETSI, Seville, Spain, to increase renewable energy use in future studies.

Policies have been increasing investments and knowledge development to solve the energy problem, considering fossil fuel burning continues to worsen the climate crisis. The reason is that CO_2 emissions from the energy and industry sectors have increased by 60% despite the United Nations Framework Convention on Climate Change in 1992 [1]. The energy sector is the primary source of global emissions, accounting for approximately 60% of global greenhouse gas emissions [2], and the building sector uses 40% of the world's energy production, which 5% is for cooling. Furthermore, the cooling demand tends to grow due to a hotter climate [3]. In this line, investments of 7.4 trillion euros are estimated, in the next 25 years, for the deployment of technologies that eliminate net CO_2 emissions [3]. Therefore, solar cooling technologies development is a clever way to reduce the CO_2 emissions while enhancing cooling plants' technological maturity and economic viability [4]. Thus, solar cooling technology has received much attention [5].

Solar absorption plants produce cold from a solar-heated source through an absorption thermodynamic cycle [6]. It has the feature of having solar energy availability following the cooling demand. The problem is that using solar energy as the primary source adds the complexity of having a process that is intermittent during the day, night, and year seasons. Besides, solar irradiance that strikes the absorber is subject to clouds that strongly affect the plant's dynamic behavior. Thus, generating a stable heat source for the absorption chiller is critical.

* Corresponding author at: US - Universidad de Sevilla. Departamento de Ingeniería de Sistemas y Automática, Camino de los Descubrimientos, Sevilla, 41092, Andalucía, Spain.
E-mail address: bordons@us.es (C. Bordons).

https://doi.org/10.1016/j.apenergy.2023.120944
Received 4 August 2022; Received in revised form 9 December 2022; Accepted 5 March 2023
Available online 17 March 2023

Several concentrating solar collector types harvest thermal solar energy. Parabolic Trough Collectors (PTC) and Fresnel Solar Collectors (FSC) are among the line focus systems. Despite PTC's technological maturity and higher efficiency, the FSC has advantages compared to PTC [7], mainly cheaper production resulting in equivalent Levelized Cost of Electricity. Besides, FSC has room for further technological development [5,7]. In this way, improving the technological/economic performance of these systems [8] is highly desirable [9]. This work seeks to improve FSC operation through its Digital Twin formulation for future control and optimization studies.

From the whole plant control perspective, a hierarchical structure typically solves the scheduling (integration), optimizing (plan), and controlling problems, separating them into layers considering the computation effort and operation horizon of each one [10]. The upper optimization layers minimize a given cost function and send the optimal schedule or operation points solution to the control layer. The control layers seek stable operation, reference tracking, and disturbance rejection. The optimization layers typically use the Real-Time Optimization (RTO) technique [11], while the multivariable control layer uses Model-based Predictive Control (MPC) techniques [12]. Both run models continuously in a feedback loop. Therefore, the model's accuracy directly impacts the control, optimization, thus, the process operation.

Specifically for concentrating solar collectors that operate intermittently, with a wide operational range, and present slow and fast dynamics, a typical RTO with non-linear steady-state models and a linear MPC with dynamic models presents limitations [13–15]. With this, the dynamic models resulting from this work are accurate for both steady-state and dynamic optimizations with low computational burden, enabling assets for control and optimization [16,17]. These models facilitate more advanced techniques realizations, feasible in shorter sampling times, such as DRTO [18], Economic MPC [19], or hybrid approaches [20].

A Digital Twin (DT) has many definitions. In a review study, Rasheed et al. [21] state that a Digital Twin is a "virtual representation of a physical asset enabled through data and simulators for real-time prediction, optimization, monitoring, controlling, and improved decision making". Although the concept, its definition, and the related studies continue to evolve in many areas [22]. Digital Twin is one of the most promising enabling technologies for Industry 4.0 viability, already having applications in the industry through publications, patents, and best practices of leading companies. The applications cover product lifecycle, product design, reliable/flexible production, prognostics, and health management [23]. The application of DT in the energy sector is relatively scarce. Rasheed et al. [21] compiles DT contributions to the energy sector, having studies on asset maintenance, energy saving, improving efficiency in smart factories aiming to reduce both production costs and greenhouse gas emissions, design, construction, and performance of residential buildings. Although, only one study published a full-scale DT of a district heating and cooling network. As can be seen, a core DT enabling technology is the modeling, simulation, verification, and validation.

This paper develops both physical and data-driven models of the Fresnel Solar Collector (FSC) of *Escuela Técnica Superior de Ingeniería de Seville* (ETSI), Spain, to compose its DT. A validation states their performances considering the computational execution time and statistical indexes. The plant location is on the roof of the ETSI building. It aims to supplement the air conditioning system with chilled water to reduce electric consumption, CO_2 emissions, and operating costs [24]. The plant is a multi-energy system once it transforms solar irradiance into internal thermal energy, hot water into chilled water (thermal to thermal), and gas chemical energy into internal thermal energy. This system is also complex, highly non-linear, and dynamic, switching between electric, gas, and solar resources according to meteorology and demand profiles. The objective is to integrate and enhance the energy system with control [25], and optimization techniques [26].

It is worth noting that the ETSI plant is a physical entity. It has computers, servers, and industrial communication structures to connect virtual and physical spaces. Thus, the only asset not available for the ETSI absorption plant DT is its adaptive virtual entity or its adaptive dynamic model. This work seeks to expand the ETSI FSC model with the following specifications:

1. To consider the transitory regime, the continuous focus/defocus of the mirrors, and the cleanliness factor.
2. To have defined accuracy and precision indexes through validation with a representative amount of data.
3. To run fast enough to be used in Model Predictive Control (MPC) techniques.
4. To describe transients, and part-load, during the day and night for control, optimization, and what-if decisions.
5. To adapt and cope with the aging of the FSC for updated plant operation, long-term, and lifecycle assessment.

These specifications have the following justification. Describing the solar collector considering day and night is especially important because solar plants are intrinsically intermittent and have appreciable heat losses during the night. Thus, this model feature can aid start-up/shut-down decision-making, contributing to optimal thermal storage strategy formulation [24]. The focus/defocus action is critical for the safety [27] and control [28] of FSC. However, to the best of the authors' knowledge, there is no FSC validated model with the defocus feature. The cleanliness factor is related to thermal efficiency and varies over time. Thus, a model that can adapt such parameters is necessary to predict when to stop the FSC for maintenance and cleaning [27]. Stating the model's accuracy and precision with mean error and standard deviation, among other statistical indexes, gives information about the models' confidence and the fidelity level of DT's simulations and what-if analysis [21,29–31]. The updating/adapting procedure of the virtual entities/models is called twinning. The twining is synchronizing the virtual and physical entities [29], measuring the physical entity state, and updating the virtual entity to reduce the difference between them. This process can occur either from physical-to-virtual or virtual-to-physical spaces, in a closed loop, with a twinning rate. To the authors' best knowledge, no published FSC dynamic model is available considering such features. A specific literature review about the available modeling of FSC on the ETSI absorption plant leads to the following works:

Robledo et al. [32] develop a phenomenological lumped parameter dynamic model considering the optical and thermal models and an ordinary differential equation. The authors used least-squares methods to identify the model's parameters. The validation considered four operation days data, with a 7.5 h duration each. The validation outlet temperature range is from 85 to 165 °C, and the results are qualitatively presented, contrasting the actual data and model output plots.

Spoladore et al. [33] develop a phenomenological, distributed parameters, dynamic model, considering the optical and thermal models and Partial Differential Equations (PDE). The authors used least-squared methods to identify the global heat loss and the metal-fluid heat transmission coefficients considering second-degree polynomial functions. The validation considered two operation days data from 11:00 to 18:00, on May 27, 2010, and November 17, 2009. The outlet temperature ranges from 100 to 180 °C, with a maximum error of 8 °C. The authors present qualitative comparison plots between model prediction and actual data.

Pino et al. [27] develop phenomenological, steady-state, thermal, and optical models using algebraic equations that account for the focus of the mirrors. The validation considers the mirror's rows inclinations, absorbed heat, and outlet temperature during operation between 13:00 and 15:30 on May 27, 2009. The validated outlet temperature range is from 147 to 168.5 °C, with relative errors of less than 1%.

Chicaiza et al. [34] develop data-driven dynamic models based on Adaptive Neuro-Fuzzy Inference System (ANFIS) to compose a DT. The

ANFIS training considers two days of actual and artificial data from PDE models. The validated outlet temperature range is from 40 to 180 °C in three days of actual data. The authors present qualitative plots between measured and model outlet temperatures and calculate the Root Mean Squared Error (RMSE) and the Mean Absolute Percentage Error (MAPE) for each day. The worst-case RMSE = 12.96 °C and MAPE = 8.54%, while the best-case RMSE = 3.67 °C and MAPE = 2.27%.

Considering the previous works on the ETSI FSC modeling, this paper has the following contributions.

1. It develops dynamic models using both ANFIS [35] and PDE [36] to generate a transparent model with explicit equations and expand FSC models capabilities. This work uses 25 days of operation data with a sampling time of $t_s = 20$ s, with continuous data between day and night.
2. The ANFIS twinning (training and checking) and validation consider 19 days of measured data. On the other hand, identifying PDE model parameters uses four days of measurement data re-sampled every 5 s to avoid numerical integration instability. The massive amount of data in twinning results in generalized dynamic models of both ANFIS and PDE.
3. The validation procedure considers six days of actual operation data, three in June and three in October. The validation results indicate that the models can adequately represent the behavior of the FSC outlet in a wide temperature range, from 40 to 180 °C.
4. The models describe operations continuously during day and night, part-load operations, or overnight, with heat losses.
5. To the best authors' knowledge, this work presents the first FSC-validated dynamic models that describe the mirror's focus/defocus action.
6. Lastly, this work contributes to testing the computational speed of resulting dynamic models during twinning and simulation, setting the execution time limits of the models regarding MPC and dynamic optimization techniques.

The organization of the rest of the paper is as follows. Section 2 defines the FSC process and presents the actual data preparation and its correlation analysis, closing with the FSC operation description. Section 3 presents the FSC phenomenological distributed parameters modeling and its identification. Section 4 states the ANFIS architecture and defines its training procedure. Section 5 defines the simulation planning with the model structure definition and data sets preparation. Section 6 states the results divided into two parts, the first is the twinning time of both models (training and identification), and the second is devoted to validation results and indexes considering actual data. Lastly, Section 7 shows the findings of this work and closes the paper.

2. Fresnel solar collector process

The Fresnel solar collector (FSC) installed at ETSI was constructed by PSE AG, which activities have passed to Mirrox Gmbh, and today is Industrial Solar [37]. Fig. 1 depicts the referred Fresnel concentrating solar collector that generates heat for an absorption chiller that, in its turn, supplements the building air conditioning system with a renewable primary energy source. The solar field has an 18° orientation in the east–west direction, a total area of 352 m^2, where 11 mirror rows and 16 modules compose the optical system, summing 64 m of length, which focus the solar irradiance to the receiver as depicted in Fig. 2. The receiver, in its turn, is composed of a secondary reflector and an absorber tube, where glass thermal insulation equips both. Steel DNI 1.4541 (AISI321) composes the SCHOTT PTR70 [38] absorber tube, installed 4 meters above the mirror's plane.

Water is the heat transfer fluid and flows inside the absorber tube, with 13 bar and 180 °C of nominal pressure and temperature, respectively. Table 1 presents the main characteristics of the Fresnel solar collector.

Table 1
ETSI Fresnel solar collector characteristics [24,38].

Parameter (symbol)	Value	Unit
Total area	512	m^2
Total mirror area (A_t)	352	m^2
Absorber length	64	m
Absorber height	4	m
Mirror unitary length	4	m
Mirror unitary width	0.5	m
Total Mirror aperture (G)	5.5	m
Mirrors rows	11	–
Number of mirrors	176	–
Absorber tube specific mass (ρ_m)	8027	kg/m^3
Absorber tube external diameter	0.07	m
Absorber internal diameter	0.066	m
Absorber tube specific heat (c_m)	500	J/(kg °C)
Receiver cavity aperture	0.3	m
Heat transfer fluid	Water	–
Nominal temperature	180	°C
Nominal pressure	13	bar
Nominal thermal power	120	kW

The FSC objective is to generate a hot outlet temperature flow. The incident irradiance and the inlet temperature are critical disturbances of the solar collector process because they fastly and widely affect the outlet temperature. The plant start-up occurs when the solar irradiance reaches a minimum, starting the pump, mirror's sun tracking, and focusing the solar beam into the absorber tube. After this beginning, the controller manipulates the flow and the mirror's focus to regulate the outlet temperature of the collector with the objectives of reference tracking and disturbance rejection. The plant's shut-down occurs when irradiance reaches a given minimum value.

2.1. Data preparation

Neuro-fuzzy (NF) and Partial Differential Equations (PDE) models are identified and validated using actual data for predicting the FSC dynamic behavior. Therefore, an identified model is only as good as the data used to fit/train it [39]. The impact of feeding the identification system and validating with poor-quality data is low accuracy and veracity, leading to pointless work and unuseful results that, if used, would result in economic and safety losses [40]. Thus, data preparation means the model is built right [41].

Data quality assessment uses accuracy, completeness, consistency, and timeliness classifications [42]. This work executes the following preparation seeking these classifications: filtering instrumentation noise, homogenizing sampling times, excluding data garbage, and carefully choosing variables that affect the process. The preparation strongly affects the model's accuracy in the results section.

This work employs raw data from the solar absorption plant's SCADA system that stores measurements in Excel data sheets daily. Each file has 18 variables (columns) imported to Matlab as timetables with the respective headers or variable names. An algorithm tests each Excel sheet header to maintain the same variables' order names to avoid mixing different variables in one array. Then each available day of operation was concatenated by time, considering consecutive days. Data inspection indicates incomplete data, missing measurement values, and irregularly sampled data.

The data preparation consists of re-sampling the initial timetables using linear interpolation, defining the new sample as the statistic mode of raw data sampling times, which is $t_s = 20$ s. It is worth noting that the sampling time of 20 s repeats in more than 96% of the raw data. Therefore, the plant's automation system has this sampling time which the authors maintained for homogenization. After the data import and re-sample procedure, it passes through a concatenation, resulting in eight regular timetables: from June 9th to 12th, 23rd to 26th, 29th to 30th, August 11st to 12th, 14th to 17th, September 2nd to 3rd, 22nd to 25th, and October 14th to 16th, totaling 25 days of operational data.

Fig. 1. Fresnel solar collector installed at ETSI absorption solar plant [34].

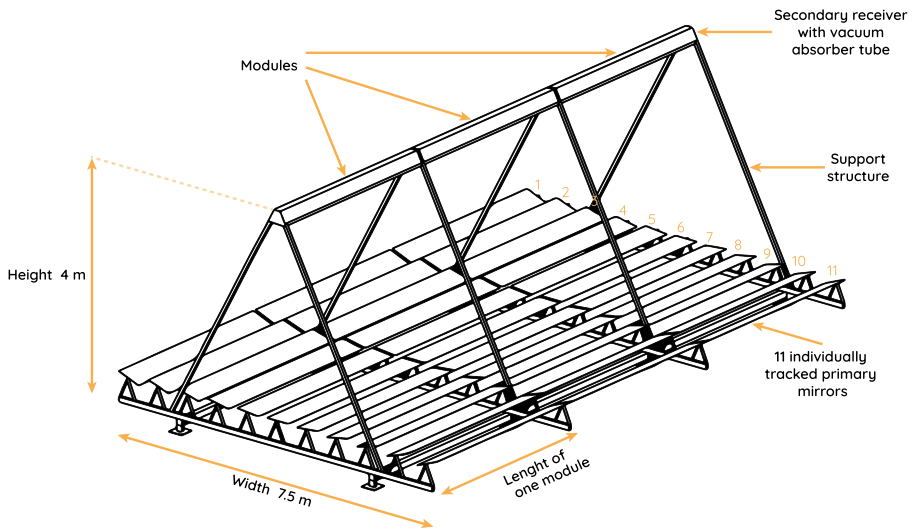

Fig. 2. Fresnel solar collector model installed at ETSI absorption solar plant [37].

Next, a moving mean filter with a 6 min window was applied to remove outliers from data sets. The window was chosen by trial and error for proper outliers detection and substitution considering a series of visual inspections of the raw data and the outliers' clean data. In addition, a one-by-one evaluation substituted negative pressures, flows, and inconsistent variables by the minimum or maximum absorption solar collector operation range considering the manufacturer's data-sheet [37]. The variable-by-variable inspection also led to the discovery of empty columns that were further deleted.

Furthermore, pressure and flow variables were smoothed using Gaussian interpolation with a 15 sampling window. The sampling window was chosen by trial and error, considering a good compromise between lag and dynamic information loss (long window) and noise (short window). As a result, 14 variables compose the final data set with 108 416 samples.

It is worth saying that the previous literature on the modeling of the FSC on the ETSI does not discuss the experimental data quality, the preprocessing, or the data preparation procedure for simulation reproducibility nor considers the intermittent operation of the plant

with the same amount of data points. These differences highlight an important improvement in FSC modeling in this work. The following section presents the data selection based on correlation maps.

2.2. Correlation analysis of FSC field I/O variables

The correlation coefficient measures the association between variables, the most widely used is the linear correlation coefficient. Pearson's correlation coefficient (ρ) for pairs of variables $(\mathbf{x}, \mathbf{y})$ with n samples $\mathbf{x} = [x_{1,1}, \dots, x_{n,1}]$ and $\mathbf{y} = [y_{1,1}, \dots, y_{n,1}]$ is given by

$$\rho(x,y) = \frac{1}{n-1}\sum_{i=1}^{n}\left(\frac{x_{i,1}-\mu_x}{\sigma_x}\right)\left(\frac{y_{i,2}-\mu_y}{\sigma_y}\right), \tag{1a}$$

$$\mu_x = \frac{1}{n}\sum_{i=1}^{n} x_{1,i}, \tag{1b}$$

$$\sigma_x = \sqrt{\frac{1}{n-1}\sum_{i=1}^{n}(x_{1,i}-\mu_x)^2}, \tag{1c}$$

where μ_x and σ_x are the mean and standard deviation of the samples of $\mathbf{x}$, respectively, and μ_y and σ_y are the mean and standard deviation of $\mathbf{y}$. The values that ρ can take are between $[-1, 1]$, where $\rho = -1$ represents a complete negative correlation, $\rho = 1$ represents a complete positive correlation, and a value of $\rho = 0$ indicates that the variables $(\mathbf{x}, \mathbf{y})$ are uncorrelated.

The correlation coefficient matrix ($\mathbf{R}$) of the random variables M is $\mathbf{R} \in \Re^{M\times M}$ for each combination of pairwise variables. Only for x and y, result in the following matrix $\mathbf{R} \in \Re^{2\times 2}$:

$$\mathbf{R} = \begin{pmatrix} \rho(x,x) & \rho(x,y) \\ \rho(y,x) & \rho(y,y) \end{pmatrix} = \begin{pmatrix} 1 & \rho(x,y) \\ \rho(y,x) & 1 \end{pmatrix}. \tag{2}$$

The next step is sorting the input variables in a degree of relationship. The sort evaluates the degree of correlation for each input regarding the desired output to analyze which variables impact the model output concerning a threshold. In the case of FSC, the desired output is the outlet temperature $Tf2$. Fig. 3 shows the correlation coefficient matrix of the actual Fresnel solar field data. Where f is the mirrors' focus, varying between 0 for full defocus to 1 for complete focus; q is the volumetric flow, P is the hydraulic pressure, $Tf1$ and $Tf2$ are the inlet and outlet temperatures, respectively; ws is the wind speed, I is the solar irradiance, H is the humidity, $Tamb$ is the environment temperature. $EffOpt$ is the optical efficiency accordingly to Brandão et al. [43], and $Tf1\ delay$ is the delayed inlet temperature calculated accordingly to Normey-Rico et al. [44].

2.3. FSC operation

Fig. 4 depicts the main operation variables from the prepared data considering two operation days: from June 24, 06:00, to June 26, 00:00, 2009. It is worth saying that the validation section uses the same exact actual data.

By inspecting Fig. 4.a, one can see two days of irradiance profile. The irradiance profile (continuous yellow line) of June, 24, is smooth, with the sunrise at about 06:00, a peak at 15:00, and the sunset at 22:00. The operation stages follow the irradiance profile, where the start-up occurs when there is enough irradiance, $I \geq 200$ (W/m^2), at almost 09:00 turning on the pump, see Fig. 4.b. Note that the flow goes from 0 to 13 m^3/h together with the mirror's focus from 0 to 100%. Next, the heating phase occurs with the FSC increasing its temperature from 09:00 to 12:00. Then, the absorption chiller consumes the FSC thermal power. It generates a sudden temperature drop followed by a temperature increase return between 12:00 and 14:00. The temperature drop results from the absorption chiller's lower internal temperature injection in the FSC hydraulic loop. After a recovery period, the temperature increases again due to the gas boiler operation.

After the absorption chiller start-up, aided by the backup gas boiler from 12:00 to 14:00, the boiler is shut-down. The plant operates roughly at the nominal point with solar irradiance only, producing chilled water for the ESTI air conditioning system. Note that the temperatures are highly oscillatory from 14:00 to 20:00 due to the absorption chiller on–off controller operation. The two-position valve effect is evident in the hydraulic loop flow (blue dotted line) in Fig. 4.b, where F varies between two levels during operation. This bi-stable event happens because when the controller feeds the chiller High Temperature Generator, a heat exchanger with long tubes generates a pressure drop reflecting the flow changes in Fig. 4.b. For further information on the whole plant control logic, refer to [28].

When the irradiance is too low, that is I $\leq$ 200 (W/m^2), the flow and mirror's focus go to zero. That is why the plant shuts down at 20:00. Then, from June 24, 22:00, to 25, 09:00, the FSC temperatures decrease overnight, see Fig. 4.a. After these heat losses, the operation is re-started on June 25, at 09:00, where the sequence of the same events as the previous day happens. It is worth noting that the irradiance profile of June 25, unlike the previous day, is very oscillatory.

Fig. 4 depicts the operation data of the ETSI absorption plant. The process is complex, highly non-linear, and intermittent, with a broad operational range of the variables, such as temperatures, flows, and solar irradiance. Thus, developing the FSC digital twin is not trivial, and the respective models must cope with and describe such a wide range of operations and phenomena to reflect the dynamic behavior of the FSC. After the FSC digital twin creation, it allows for optimizing the start-up, operation, and shut-down, considering changing meteorological and plant conditions while offering accurate predictions for model-based predictive control techniques. The following sections present the two model structures used in this work.

3. Phenomenological - PDE modeling

Partial differential Eqs. (3) and (4) describe mathematically the Fresnel's temperature distributed in time and space [36].

$$\rho_m c_m A_m \frac{\partial T_m}{\partial t}(t,x) = \dot{Q}_{sun}(t) - \dot{Q}_a(t,x) - \dot{Q}_f(t,x), \tag{3}$$

$$\rho_f c_f A_f \frac{\partial T_f}{\partial t}(t,x) + \rho_f c_f q(t)\frac{\partial T_f}{\partial x}(t,x) = \dot{Q}_f(t,x), \tag{4}$$

where the sub-indexes m, f, sun, and a refer to the metal absorber tube, fluid, the sun, and the environment, respectively. The variable ρ is the specific mass (kg/m^3), c is the specific heat (J/(kg °C)) and q is the volumetric flow (m^3/h). Variable T, is the temperature (°C), t is the time (s), $x \in [0, L]$, with $L > 0$, is the space (m), $\dot{Q}_{sun}$ is the sun heat rate (W) that flows from the sun to the solar collector, $\dot{Q}_a$ represents the thermal losses (W) to the ambient, and $\dot{Q}_f$ is the heat rate (W) that relates to the mass flow. Eq. (5) gives the boundary condition of Eq. (3),

$$T(t,0) = Tf1(t), \tag{5}$$

where $Tf1$ is the Fresnel inlet temperature. Finally, the initial conditions of the system are given by Eq. (6)

$$T_m(0,x) = T_m^0(x), \qquad T_f(0,x) = T_f^0(x), \tag{6}$$

where T_m^0 and T_f^0 are functions that satisfy the steady state condition of Eqs. (3) and (4).

Papers in literature use the system of Eqs. (3)–(6) for both parabolic through and Fresnel collectors. The difference among the different solar collector's equations is mainly in calculating the optical efficiency η_{opt} once each type of solar collector has a specific primary and secondary mirrors scheme [45]. The optical efficiency is in the inlet solar heat term, $\dot{Q}_{sun}$, which Eq. (7) describes,

$$\dot{Q}_{sun} = \eta_T \eta_{opt} A_t I(t), \tag{7}$$

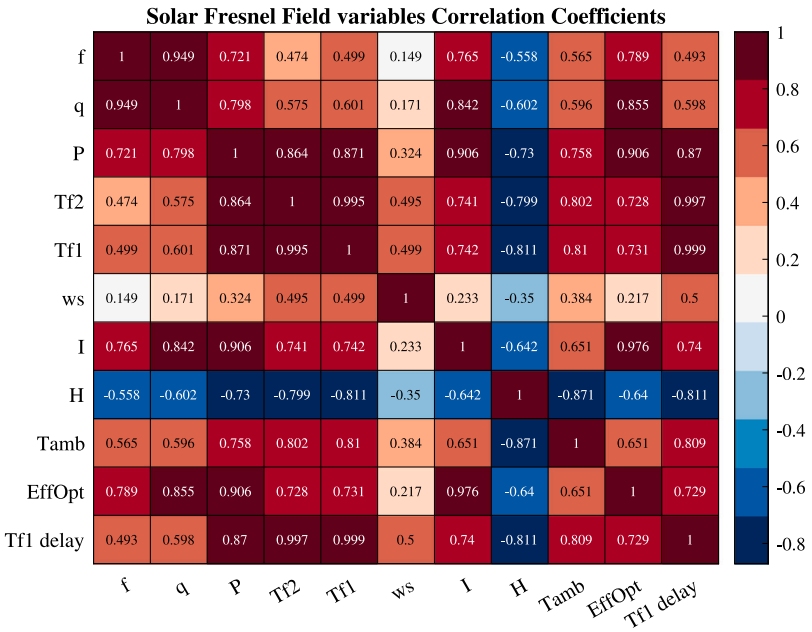

Fig. 3. Correlation coefficients matrix of the prepared ETSI FSC field data.

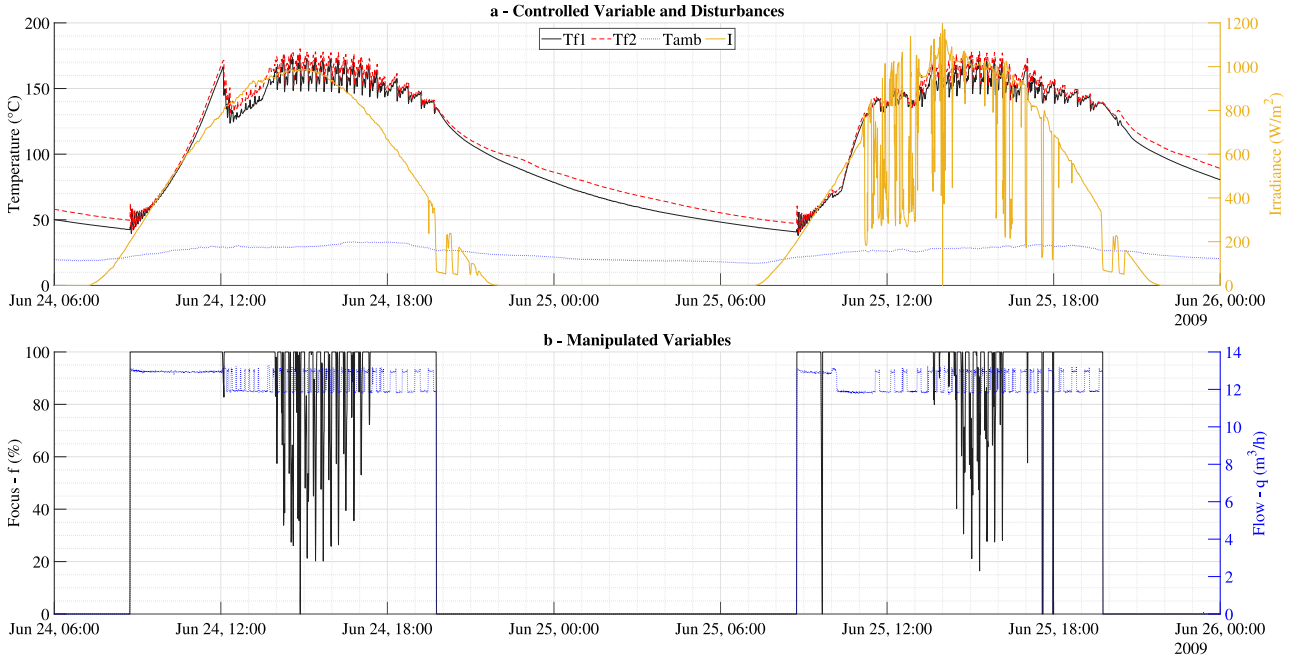

Fig. 4. FSC consecutive days operation actual data. a. The FSC outlet temperature $Tf2$ is the controlled variable, while the inlet temperature $Tf1$ and Irradiance I are the prominent disturbances. b. The FSC installed at ETSI has two manipulated variables, the typical flow q, and the mirror's focus f.

where η_T and η_{opt} are the thermal and optical efficiency, respectively, $A_t(\mathrm{m}^2)$ is the total area of collector's mirrors, and I is the solar irradiance per mirror length in $\mathrm{W/m}^2$.

A Fresnel efficiency has both variable and constant parameters in time. For example, having a given collector's orientation and solar time enables one to calculate the solar beam's incidence angles and the respective reflection cosine losses. However, the reflexivity and other characteristics of the mirrors vary with plant aging, dirt accumulation, and water condensations in the mirrors. Thus, this work considers that the variable η_{opt} contains the deterministic and constant parameters, which are calculated accordingly to Brandão et al. [43], considering the geometrical relation between the mirrors and absorber. With η_{opt} is possible to calculate the equivalent irradiance that arrives in the absorber tube $I_{eq} = I(t)\eta_{opt}$. The time-varying and, a priori, unknown efficiency-related parameters are embedded in one unique parameter called thermal efficiency η_T, which this work estimates using an identification technique.

This work applies Euler's finite differences discrete approximation, according to Fig. 5 schematic, to solve Eqs. (3) and (4), that are continuous in time and space. The spatial derivative in a given time instant is given by

$$\frac{\partial T_f}{\partial x}(t,x) \approx \frac{T_f(t,n) - T_f(t,n-1)}{\Delta x},$$

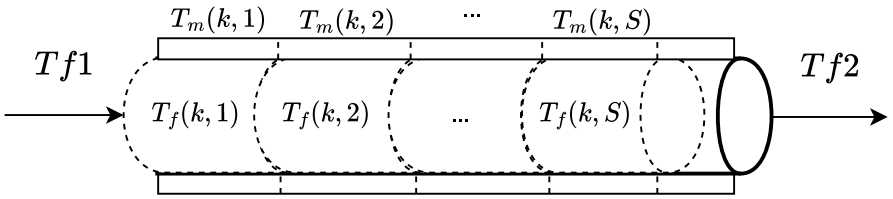

Fig. 5. Absorber tube discretization considering S = 16.

where $\Delta x = L/S$ is the length of the spatial discretization, S is the number of points, and $n \in \{1, \dots, S\}$ is the respective given volume. Note that $T_{i,0} = Tf1(t)$, as Eq. (5) presents.

Constant time intervals, M, composes the whole time horizon $t \in [0, t_f]$, where t_f is the final time, such that $\tau_k \in [0, t_f]$, $k = \{1, \dots, M\}$, are points in the discretization mesh concerning the time, with

$$0 = \tau_1 < \cdots < \tau_{M-1} < \tau_M = t_f.$$

This discretization is considered equidistant for simplicity. Thus,

$$\Delta t = \frac{t_f}{M-1}, \qquad \tau_k = (k-1)\Delta t, \qquad k \in \{1, \dots, M\}.$$

and the time derivatives approximations are

$$\frac{\partial T_m}{\partial t}(t,x) \approx \frac{T_m(k+1,x) - T_m(k,x)}{\Delta t},$$
$$\frac{\partial T_f}{\partial t}(t,x) \approx \frac{T_f(k+1,x) - T_f(k,x)}{\Delta t}.$$

The derivative approximations in time and space above transform Eqs. (3)–(4) in algebraic discrete Eqs. (8) and (9)

$$T_m(k+1,n) = T_m(k,n) + \Delta t\left(\frac{\dot{Q}_{sol}(k)}{\rho_m c_m A_m} - \frac{\dot{Q}_a(k,n)}{\rho_m c_m A_m} - \frac{\dot{Q}_f(k,n)}{\rho_m c_m A_m}\right), \tag{8}$$

$$T_f(k+1,n) = T_f(k,n) + \Delta t\left(\frac{q(k)}{A_f}\frac{T_f(k,n) - T_f(k,n-1)}{\Delta x} + \frac{\dot{Q}_f(k,n)}{\rho_f c_f A_f}\right), \tag{9}$$

where

$$\dot{Q}_a = D_m \pi [a(T_m(k,n) - T_a(k))^3 + b(T_m(k,n) - T_a(k))], \tag{10}$$

$$\dot{Q}_f = D_f \pi Ht(T_m(k,n) - T_f(k,n)), \tag{11}$$

$D_m(m)$ is the equivalent diameter of the tube walls, $D_f(m)$ the internal tube diameter, a and b are the coefficients of heat losses of the absorber polynomial function, and H_t(W/(m °C)) the coefficient of heat transfer between the tube walls and the fluid.

It is worth noting that this paper proposes a third-order heat loss polynomial function to describe the heat losses coefficient, Eq. (10), instead of fourth and second-order polynomials that are typically used [32,33]. The third-order polynomial is employed because it becomes possible to change the sign of $\dot{Q}_a$ of Eq. (10), and consequently, the heat losses term of Eq. (8). That is, by using a third-order polynomial, the tube model can also represent the case where the heat enters the tube instead of exiting. The case where the tube receives heat occurs if the plant does not operate for days. Therefore, the tube's temperature tends to be ambient temperature. In this case, it is possible that $T_m < T_a$. Thus, the model can reproduce the plant's dynamic behavior in real-time, becoming a tool for what-if analysis of the start-up and shut-down of the plant independently of the state of the process after day and night of operation.

To integrate Eqs. (8) and (9), it is necessary to iterate $T_m(k+1,n)$ and $T_f(k+1,n)$ from the initial and boundary conditions given in $T(0,n)$ and $T(k,0)$, respectively, from n = 1 to n = S, and from k = 1 until k = M. This work employs the *ode45* package of MATLAB [46] to integrate the phenomenological model.

3.1. Identification

The previous section has presented the FSC's model considering phenomenological concepts and, therefore, the main dynamics that occur in the plant. The model has thermodynamical characteristics such as specific mass, specific heat, and heat transfer coefficients between the heat transfer fluid, the metallic tube, and the environment. Despite knowing these parameters for pure substances and materials references, the values can vary sensibly due to the plant aging, corrosion, mirror soiling, and internal pipe walls crusting. Thus, these parameters are time-varying; thus, it is necessary to identify their values to plug in the model for representing the process in a given time regarding the data used for identification.

One advantage of Eqs. (8) and (9) is the possibility to estimate the parameters' values by comparing the model output with experimental data. The estimation employs a quadratic non-linear minimization algorithm through Eq. (12) to adjust the proposed model parameters. The cost function is the sum of the normalized quadratic error between the Fresnel model predicted outlet temperature, $T_f(k,64)$, and the measured outlet temperature, $T_f^*(k)$. The model's parameters are the decision variables of the optimization problem, with the initial points and maximum bounds set considering experimental and manufacturer data.

For $n \in \{1, \dots, S\}$, Eq. (12) defines the optimization problem:

$$\min_{\eta_T, \rho_f, c_f, a, b, Ht} \sum_{k=1}^{M} \frac{(T_f(k,64) - T_f^*(k))^2}{T_f^*(k)^2}$$

subject to,

$$\begin{aligned}
&\text{Eq. (8)},\\
&\text{Eq. (9)},\\
&T_m(0,j) = T_m^0(j),\\
&T_f(0,j) = T_f^0(j),\\
&T_f(k,0) = Tf1(k),\\
&0 \le \eta_T \le 1,\\
&800 \le \rho_f \le 1000,\\
&4200 \le c_f \le 4500,\\
&0 \le a \le \infty,\\
&0 \le b \le \infty,\\
&353 \le Ht \le 2500,
\end{aligned} \tag{12}$$

where $M = 207\,605$ is the number of measurements, the lower and upper bounds were chosen based on the materials' physical parameters and properties tables. Each Eq. (12) iteration integrates Eqs. (8) and (9) along the tube, from 1 to S, and the time, from 1 to M. The code execution continues until the stopping criteria condition. Such conditions are the maximum number of iterations and the objective function derivative convergence to a minimum constant value.

The *fmincon* [47] Matlab's algorithm solves the model parameter identification problem. The decision variables are the thermal efficiency η_T, the specific mass of the fluid ρ_f, the polynomial coefficients a and b of thermal losses regarding Eq. (10). Lastly, Ht is the heat transfer coefficient between the metal and water. The identification procedure

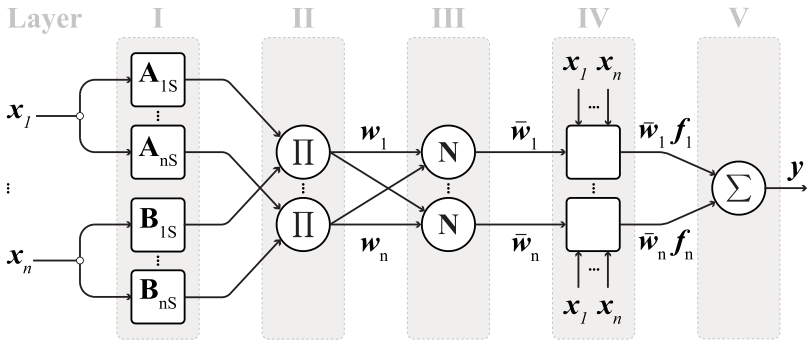

Fig. 6. Adaptive Neuro-fuzzy Inference System (ANFIS) architecture [35].

considers that all parameters are equal along the tube length. Besides, the simulation considers steps of 5 s to avoid numerical instability; therefore, it is necessary to interpolate the input data accordingly. Section 6.1 discusses the identification results of the FSC parameters.

4. Neuro-fuzzy modeling

The modeling of a system to faithfully represent its behavior has a certain level of complexity due to the random dynamics of the unknown nature of the process, making it a challenge to describe its behavior utilizing mathematical equations. Often an accurate model will be represented by several mathematical equations. However, a model supported by mathematical tools (e.g., differential equations) is only sometimes adequate to deal with uncertain systems. In addition, developing control and optimization strategies using nonlinear models to obtain the system prediction implies a high computational burden. It is the principal hindrance if the problem must be solved in a given constrained time, considering the sampling time, so a fast model is indispensable.

Fuzzy models have proven to be an effective technique for modeling and controlling nonlinear systems, successfully expressing the original nonlinear model as a set of local linear models interpolated by a membership function containing the nonlinearities of the original model. In addition, fuzzy inference systems (FIS) describe the behavior of a process based on rules with linguistic labels from human language. Thus, FIS represents the qualitative aspects of human knowledge and reasoning processes, avoiding precise quantitative analyses.

The ANFIS architecture [35], also called the Neuro-Fuzzy (NF) system, is an artificial intelligence (AI) technique. One ANFIS has five layers, as depicted in Fig. 6, where the nodes of the first (I) and fourth layers (IV) have adaptive (square blocks) parameters, and the remaining layers have fixed parameters (circle blocks). The first layer contains the fuzzification interface, which transforms a crisp input into linguistic labels with a certain degree of membership, forming the fuzzy sets [48,49] characterized by the membership functions (MF). The parameters are adaptive and are called *antecedent parameters*. The second layer outputs the product of the incoming signals from each fixed node and represents the firing strength of each node rule. The third layer normalizes the output of each node, calculated as the ratio of the firing strength of the node's rule to the sum of all the firing strengths of each node rule. In the fourth layer is the defuzzification interface, and each node function provides the weighting of a first-order polynomial crisp function, whose parameters are called *consequent parameters*. Lastly, the fifth layer contains a single node aggregating all rule outputs. For a detailed description of the ANFIS architecture network, refer to [35,50].

4.1. Training of ANFIS

The resulting FIS, after training, contains a set of rules of Takagi–Sugeno [51] type as the following:

$$\texttt{IF } x_1 \texttt{ is } F_{1j} \texttt{ and } x_2 \texttt{ is } F_{2j} \texttt{ and } x_i \texttt{ is } F_{ij}\ ,$$

$$\texttt{THEN}: f_j(x) = g_{0j} + g_{1j}x_1 + \cdots + g_{ij}x_i.$$

Each rule has an antecedent and consequent parameter. The fuzzy sets F_{ij} of each crisp entry x_i consist of Gaussian membership functions of the type:

$$\mu_{F_{ij}}(x_i) = \frac{1}{1 + \left[\left(\frac{x_i - c_{ij}}{a_{ij}}\right)^2\right]^{b_{ij}}} \tag{13}$$

where $\{a_{ij}, b_{ij}, c_{ij}\}$ are the *antecedents parameters* that define the mean, height, and width of the Gaussian used to vary the MFs,[1] and the terms $g_{ij} \in \Re$ of each first-order polynomial function are the *consequent parameters*. The learning process of the ANFIS neuronal architecture adapts both parameters. The output of each rule f_j is a linear combination of input variables added to a constant term. The final output of the fuzzy inference system is the weighted average of each rule's output.

The learning process of the ANFIS network architecture uses the training and checking sets to capture better the system's dynamics, which allows for an acceptable model that predicts its behavior. The ANFIS uses as inputs the variables $\{I, Eff Opt, f, T_{amb}, q, Tf_1, ws, H, P, Tf_{1\,delay}\}$ and as output Tf_2, thus constructing a mapping of the input–output variables that represent the behavior of the solar field. Initially, the subtractive clustering (SC) method [52] is used to estimate the number and initialization centers of the Gaussian MF of the fuzzy rules. In addition, learning employs a hybrid learning method. The method runs a back-propagation algorithm [53] to obtain the parameters defining the MF of each fuzzy set (*antecedents parameters*). Next, the learning also executes a least-squares to estimate the terms of the first-order polynomial function (*consequent parameters*) of the output of each rule at each epoch. An epoch, or sweep, is one forward and backward parameter update.

The checking procedure evaluates the error between the ANFIS output and the actual output of the checking data set (a new data set not used in training). The checking runs after each epoch during the training and aims to evaluate if the ANFIS training results in generalized learning. If the ANFIS output has low errors with unknown inputs, then it is said that the ANFIS model had general learning. Typically, the checking considers the root mean squared error (RMSE) given by Eq. (14)

$$RMSE = \sqrt{\frac{\sum_{i=1}^{N}(x_{i,j} - \hat{x}_{i,j})^2}{N}}, \tag{14}$$

[1] The value that the function $\mu_{F_{ij}}$ takes for a given x_i is known as the degree of membership of x_i for the fuzzy set F_{ij}.

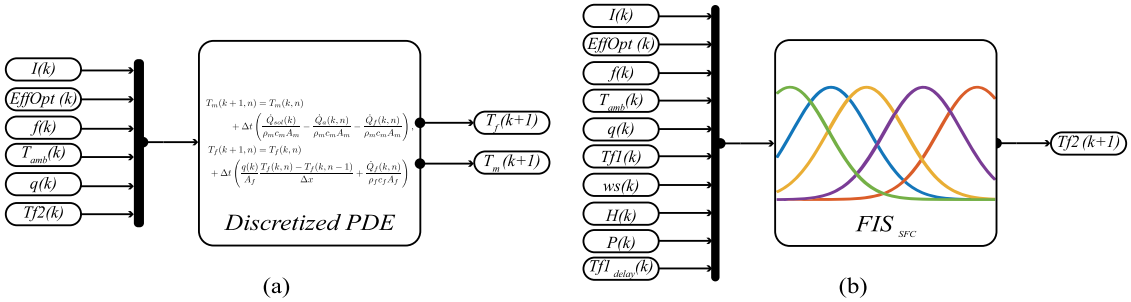

Fig. 7. a - SFC outlet heat-transfer fluid temperature PDE model. b - SFC outlet heat-transfer fluid temperature ANFIS model.

Table 2
ANFIS parameters.

Description	ANFIS
MF type:	Gaussian
Number MFs:	4
Number rules:	4
Influence range	0.8
Epoch number:	1500

Table 3
Simulation planning.

Schematic	Fig. 7.a	Fig. 7.b	Fig. 7.b
Structure	PDE(dt = 5)	ANFIS(dt = 5)	ANFIS(dt = 20)
nº inputs variables	6	10	10
nº outputs variables	T_f and T_m	$Tf2$	$Tf2$
Twinning	Par. identification	Learning	Learning
Method	LS[a]	LS and GD[b]	LS and GD
Data-set	$G_{PDE}^{Twinning}$	$G_{NF}^{Twinning}$	$G_{NF}^{Twinning}$
Data-set size	4 days	19 days	19 days
Data-set samples	14 188	311 666	78 032
Sampling time (s)	5	5	20
Stopping criteria	Eq. (12)	nRMSE[c]	nRMSE
Simulation	ODE45	1° polynomial	1° polynomial
Data-set	G^{Val1}, G^{Val2}	G^{Val1}, G^{Val2}	G^{Val1}, G^{Val2}
Data-set size	6 days of 2009	6 days of 2009	6 days of 2009
Data-set samples	95 282	95 282	23 822
Integration step (dt)	5	5	20
Validation	Table 5	Table 5	Table 5

[a]LS - Least-squares.
[b]GD - Gradient Descent.
[c]nRMSE - Normalized Root Mean Squared Error.

where $x_{i,j}$ is a given actual variable j with N samples, and $\hat{x}_{i,j}$ is the output of the predicted variable. This work considers normalized outputs ($z_{i,j}$) for training and checking. Therefore, the normalized RMSE, given by Eq. (15), is used.

$$nRMSE = \sqrt{\frac{\sum_{i=1}^{N}(z_{i,j} - \hat{z}_{i,j})}{N}}. \quad (15)$$

Table 2 presents the parameters of the ANFIS that capture the fluid outlet temperature behavior.

5. Simulations planning

This section describes the FSC PDE, and NF models structure with inputs/outputs, their twinning/updating characteristics, and validation specifications. The input selection considers the prepared data sorted accordingly to the outlet temperature $Tf2$ correlation coefficients, described in the Correlation Matrix in Fig. 3. Thus, the PDE and NF models have the structure, inputs, and characteristics summarized in 7.a and .b, respectively.

Table 3 compares Fig. 7.a PDE model and Fig. 7.b model with two different integrations steps of 5 s and 20 s. The PDE model has six inputs, while the NF model has ten inputs. This difference happens because, on the one hand, the PDE model does not describe meteorological variables such as wind speed ws, humidity H, and hydraulic circuit pressure P. On the other hand, it is easy to add these input variables to the NF model. The wind speed and air humidity affect the heating process of the Heat Transfer Fluid, changing the convective heat coefficient between the absorber tube and the environment, refer to Fig. 3. In addition, the PDE model intrinsically describes the FSC inlet temperature dead time; thus, the delayed inlet temperature $Tf1\ delay$ is employed only in the NF model. Besides, the model outputs are different. While the PDE model has two outputs vectors $T_f(k)$ and $T_m(k)$ that describe the temperature gradient along the absorber tube length, the NF model has a scalar outlet temperature output $Tf2$. It is worth noting that the PDE outputs are arrays with 16 values, where the last value represents the outlet temperature $Tf2 = T_f(16, k)$;

After defining the models' structure, the next step is twinning them to adjust their parameters to follow the plant's actual data. The PDE model is updated using least squares (LS), while the NF model uses LS and Gradient Descent (GD). The PDE model employs $G_{PDE}^{Twinning}$ as twinning data set with four days of measurement, totaling 14 188 samples. While the NF model twinning data set is $G_{NF}^{Twinning}$, which uses 19 days of data, totaling 311 666 and 78 032 samples, for sampling times of 5 s and 20 s, respectively. Refer to the middle section of Table 3 for details.

The twinning rate of a given digital twin is the updating rate of a model. Thus, knowing the twinning time of a given model is essential to defining the twinning rate of the virtual entity once the twinning rate must be lower than the models' twinning time. The twinning time is the processing time the model's twinning takes to converge the model error to a given minimum stopping criteria tolerance.

The twining data reduction for the PDE model is because the computational burden of the PDE parameter identification is high. In preliminary tests, the identification leads to more than one week of processing using the whole available twinning data set, which results in impractical twinning rates of the FSC. In addition, the sampling time was reduced to five seconds to avoid numerical instability of the PDE integration, increasing the total number of samples—see Table 3.

The re-sampling of $G_{PDE}^{Twinning}$, further PDE model updating and simulation would lead to unfair execution times compared to the NF model. Note that the latter model was initially updated and simulated, considering the prepared data with a sampling time of 20 s. Therefore, to compare the PDE and NF models updating performance, the NF model twinning is run with sampling times of 5 s, which is the same re-sampled data of the PDE model. Each column of Table 3 describes each situation, with the first column representing the PDE model with integration steps of dt = 5 s in four days of actual data, while the second and third columns have the NF model with dt = 5 s and the NF model with dt = 20 s, specifications, respectively. Both NF models use the same 19 days of actual data operation. The performance indexes for twinning are the total twinning time t_{tw}, which is the total time that it takes to update the model, the twining time per sample, $t_{tw}/sample$,

and twinning time per day of operation, t_{tw}/day, given by Eqs. (16) and (17), respectively.

$$t_{tw}/sample = \frac{t_{tw}}{t_s}, \tag{16}$$

$$t_{tw}/day = \frac{t_{tw}}{86400 t_s}, \tag{17}$$

where 86 400 is one day in seconds. Section 6.1 presents the models' performance on twinning.

After the twinning is necessary to validate the models to evaluate their performances, Table 3 summarizes the validation procedure. The NF model simulation considers MATLAB's ODE package and G^{Val1} and G^{Val2} data set that comprise almost six days of actual data. The simulations with integration steps of dt = 5 s have 95 282 samples, while the NF model simulation with dt = 20 s has 23 822 samples. It is worth noting that the NF model that uses the twinning data set with t_s = 5 s is not run in validation. Only the training procedure is done with t_s = 5 s to give a fair twinning time comparison between the models.

The validation procedure compares the model's outputs with a new validation data set of actual data, neither used for the ANFIS training nor the PDE parameter identification. The objective is to evaluate the model's ability to predict outputs, and the results are the accuracy and precision indexes of the final model. The arithmetic error mean is an index that evaluates the accuracy, or the distance between the error points and their actual center value; it is given by Eq. (18)

$$\bar{E} = \frac{\sum_{i=1}^{N}(x_{i,j} - \hat{x}_{i,j})}{N}, \tag{18}$$

and the standard deviation quantifies precision; therefore, Eq. (19) gives the dispersion of the error,

$$\sigma_E = \sqrt{\frac{\sum_{i=1}^{N}(E_{i,j} - \bar{E})^2}{N}}. \tag{19}$$

This study considers other statistical validation indexes as the standard mean error (SE), which is another measure of precision given by Eq. (20),

$$SE = \frac{\sigma_E}{\sqrt{N}}, \tag{20}$$

where SE measures how the number of samples N affects the dispersion of different datasets; as the size of the data increases, the SE decreases. Mean Absolute Percentage Error (MAPE), accordingly to Eq. (21),

$$MAPE = \frac{\sum_{i=1}^{N} \frac{|(x_{i,j} - \hat{x}_{i,j})|}{x_{i,j}}}{N} \times 100\%, \tag{21}$$

where it is a measure of the precision of a predictive system considering absolute prediction errors, $|(x_{i,j} - \hat{x}_{i,j})|$, relative to the actual measured data, $x_{i,j}$. And the coefficient of determination R^2, given by Eq. (22)

$$R^2 = 1 - \sum_{i=1}^{N} \frac{(x_{i,j} - \hat{x}_{i,j})^2}{(x_{i,j} - \bar{x}_{i,j})^2}. \tag{22}$$

where $\bar{x}$ is the mean value of the data. R^2 is a number between 0 and 1 that measures how well a statistical model predicts an outcome. If $R^2 = 0$, the model does not describe the outputs. If $0 < R^2 < 1$, the model partially predicts the outputs, and if $R^2 = 1$ the model perfectly predicts the outputs.

It is worth pointing out that the NF model validation with integration steps of dt = 5 s considers the trained model using the dataset sampled with t_s = 20 s. As will be seen in Section 6.2, this difference in sampling time of NF model twinning does not affect its accuracy.

6. Fresnel solar collector digital twins

This section presents the models' twinning results, mainly the twinning time. Then, the validation section discusses the models' performance through qualitative comparison between the models' outputs and actual data from six days of operation. Then, the performances are summarized and described using the statistical indexes presented in the previous section.

Table 4
Twinning times.

	PDE(dt = 5 s)	NF(dt = 5 s)	NF(dt = 20 s)
t_{tw} (h)	52.34	6.88	2.36
$t_{tw}/sample$ (s)	2.73	0.08	0.11
t_{tw}/day (min)	785.01	22.53	7.71

6.1. Twinning

Table 4 presents the twinning results of the models.

The NF model updated with input data sampled each 20 s has the short twinning, taking 2.36 h to update, followed by the NF model with re-sampled input data of 5 s, and finally the PDE model—see Table 4. The PDE model parameter identification is the slowest among the models, despite having fewer input data and a lower number of samples than both NF models. The PDE model's twinning time per input sample is 2.73 s, more than 20 times greater than the NF models. Updating the models with one day of operational data results in 7.71 min for the NF model with dt = 20 s, 22.53 min for the NF model with dt = 5, and 785.01 min for the PDE model. The NF model has appreciable advantages concerning mirroring the models with actual plant data. For example, updating the NF model daily at night is possible because it takes less than 7 h to do the procedure. The same does not occur for the PDE model that needs more than two days for twinning. Thus, the PDE model can be updated weekly, starting on Friday after the operation, resulting in an updated model early on Monday.

6.2. Validation and discussion

Fig. 8.a depicts the validation results for data set 1. It consists of comparing the actual measured data set G^{Val1} (continuous black line) to the PDE model (dashed red line) and to the NF model (dotted blue line).

Note on Fig. 8.a that the ETSI absorption plant has intermittent operation day and night. By inspecting Fig. 8.a, the PDE and NF models can follow the measured data profile during three days of operation. The maximum values refer to operation with sun irradiance absorption and temperature increase, while the minimum values refer to overnight heat loss and temperature decrease.

Fig. 8.b presents in detail the June 24 start-up box shown in Fig. 8.a. The plant starts when $I > 200$ [W/m^2], which typically occurs between 08:00 and 09:00 for all validation days, starting the pump that generates flow inside the absorber tube. The reason for strong oscillations in Fig. 8.b, and other day start-ups, is that the water inside the tube has a temperature gradient along the tube length that flows towards the outlet temperature sensor. This temperature distribution is affected by the day before the shut-down condition and overnight heat losses. Fig. 8.b shows that the PDE model presents less error just before the start-up than the NF model, and both models fail to represent the first start-up peak. Although after the first oscillation, the two models can successfully cope with measured data with lower error for the NF model and practically the same standard deviation among the models.

After the start-up oscillations, the outlet temperature $Tf2$ increases with the solar irradiance in the morning. The absorption chiller starts when $Tf2$ reaches the thermal load preset temperature. Feeding the chiller causes a sudden drop in the temperature ramp. See $Tf2$ profile in Fig. 8.a, before noon. The plant thermal gradient along the tubes oscillates due to the closed hydraulic loop and the absorption chiller on–off control [28]. Fig. 8.c presents the Fresnel outlet temperature profile during nominal plant operation. By inspection, the NF model has a slightly lower error, and both models have similar standard deviation ranges.

Fig. 8.d presents the plant shut-down that occurs at sunset when I < 200 [W/m^2]. The outlet temperature presents an atypical oscillation during operation on June 26 due to an absorption chiller's gas boiler

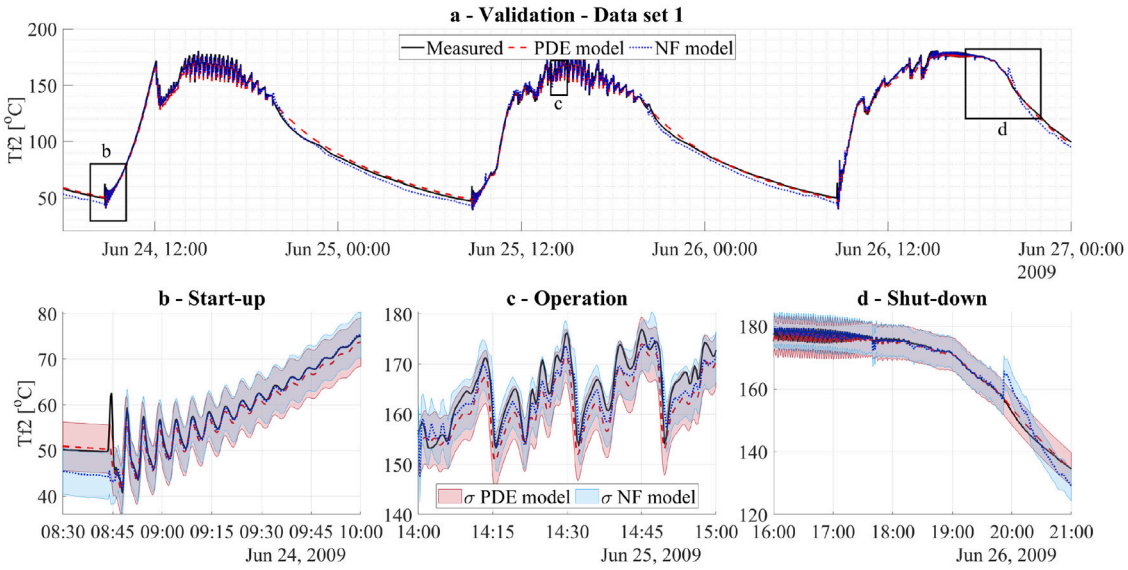

Fig. 8. a. Validation results considering data set 1 measured data (black continuous line), PDE model (red dashed line), and NF model (blue dotted line), outputs. The bottom figures b, c, and d refer to zooming the boxes at plot a. Red and blue shaded areas depict the standard deviation with 95% confidence interval ($Tf2(t) \pm 2\sigma$) of each model.

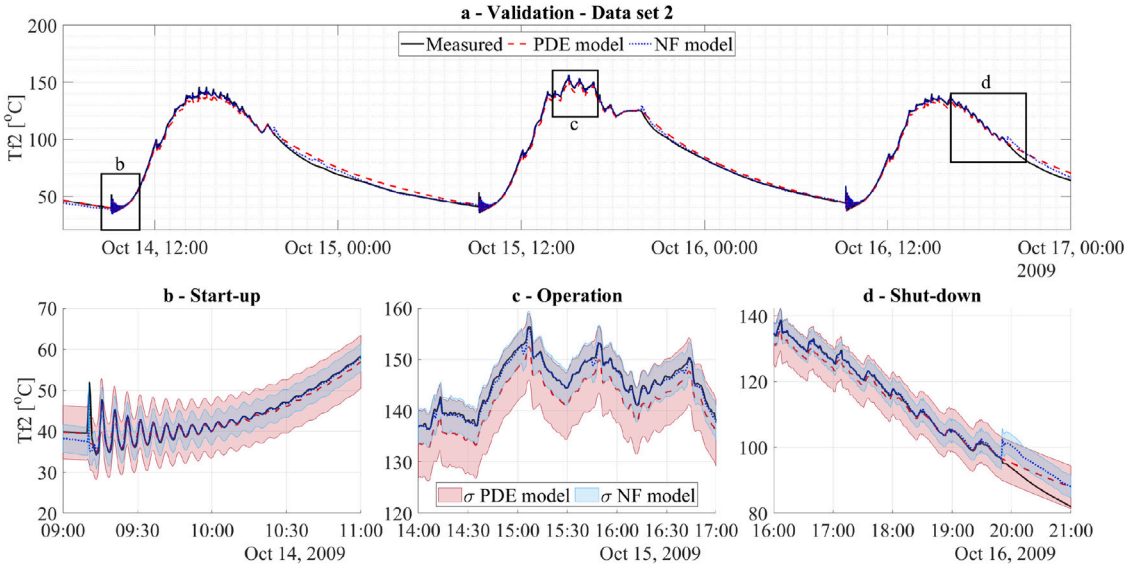

Fig. 9. a. Validation results considering data set 2 measured data (black continuous line), PDE model output (red dashed line), and NF model (blue dotted line) outputs. The bottom figures b, c, and d refer to the zoom boxes in plot a. Red and blue shaded areas depict the model's standard deviation with 95% confidence interval ($Tf2(t) \pm 2\sigma$) of each model.

use along this day. At 19:00, the $Tf2$ slope changes, and the temperature decreases more rapidly because the pump is off, and the flow goes to zero. Both models can follow the measured data, but, differently from the previous figures, the NF model has a more significant error, presenting an unusual peak oscillation at 20:00.

Fig. 9.a presents the results of validation data set 2. Compared to validation 1, validation 2 has lower maximum $Tf2$ values and oscillations amplitudes, contrast Figs. 8.a and 9.a. This difference occurs because the irradiance power is greater in June than in October. Despite different days, irradiance, and meteorological values, both models follow the measured variables on validation 2, see Fig. 9.a. A proper dynamic representation of both models in different year periods indicates that they can represent the plant dynamics in a wide operational range, from 40 to 180 °C.

Fig. 9.b presents the October 14 start-up with the same oscillatory behavior as in Fig. 8.b. The NF model is the only one capable of describing the first peak oscillation on October 14, 09:15. The NF model has lower errors than the PDE model during the start-up, operation, and shut-down. See Fig. 9.b, .c, and .d, respectively. Also, the NF model has an appreciably narrow standard deviation than the PDE model. Compare the red and blue bands, and note that the σ NF model is less than the σ PDE model.

Once both PDE and ANFIS models are obtained, they could be combined to learn from each other to enhance PDE model precision. However, an identified/trained consequent model with previous model outputs will have an accuracy equal to or lower than the previous model. Therefore, this work did not consider using the models to learn from each other because (i) actual data is available, (ii) one objective is to describe FSC transients accurately, (iii) the standard deviations are adequate, with the worst case of ±5.1 °C (Table 5).

Table 5 compiles the overall Validation 1 and Validation 2 model's index results. Note that the NF model was subject to two validation

Table 5
Validation index results.

	PDE(dt = 5)	NF(dt = 5)	NF(dt = 20)
$\bar{E}$ (°C)	−0.36	0.51	0.51
σ (°C)	2.18	2.55	2.55
2σ (°C)	4.37	5.09	5.09
SE (°C)	0.01	0.02	0.02
MAPE (%)	1.92	2.49	2.49
RMSE (°C)	2.18	2.54	2.54
R^2	0.997	0.996	0.996
t/dt (s)	0,0197	0.0034	0.0013
t/day (s)	340.28	59.14	5.79

considering different input data sampling times, one with 20 and another with 5 s. These two analyses of the NF model give a fair comparison between the simulation times regarding the PDE model that must run with integration steps of 5 s to avoid numerical problems. Note that the NF model has the same error performance despite using different integration steps, which indicates that t_s does not affect the results. The following section discusses the PDE and NF modeling error indexes.

Based on the mean error, $\bar{E}$, it is possible to infer that while the PDE model sub-estimates the outlet temperature for validation 1, the NF model super-estimates the $Tf2$ value, once $\bar{E}$ is positive and negative, respectively. The models do not present a sensible difference in the standard deviation σ, assuming a normal error distribution. The differences are almost 0.30 °C and 0.60 °C, considering 68% and 95% confidence intervals, respectively. The massive amount of samples results in low SE values, showing that the validation has an adequate number of analysis points. Lastly, the Root Mean Squared Error of PDE is 2.18 °C and for the NF is 2.49 °C, which are low values considering that the Fresnel collector has a nominal operating temperature of 180 °C. This fact is reflected in low values of Mean Absolute Percent Error of 1.92% and 2.30% for the PDE and NF, respectively. Now, closing the validation indexes discussion, the linear regression between predicted and actual FSC outlet temperatures gives coefficients of determination $R^2 \geq 0.996$ for both models. All in all, both PDE and NF models have similar error values.

Note on Table 5 that the execution time per integration step, t/dt, and execution time to simulate one day of samples t/day, show appreciable differences among the models. The PDE model takes 0.0197 s seconds to integrate one step, while the NF model, with the same integration time of $dt = 5$, takes 0.0034 s. Thus, the NF model shows almost six times faster integration step time than the PDE. These integration step times result in 61.92 s for the PDE model to simulate one day of operation, while the NF model takes 20.50 s. Thus, the NF model is three times faster. An interesting feature of the NF model is that it presents the same error levels when using integration steps of 5 or 20 s. Table 5 indicates that the NF model with a simulation step of 20 s is the faster model, simulating one day of operation more than ten times faster than the NF model using dt = 5 s and almost 60 times faster than the PDE model.

7. Conclusion

This work has developed the digital twin of a commercial Fresnel Solar Collector (FSC) installed on the roof of the ETSI building in Seville, Spain. The authors seek to create models to simulate what-if analysis, model predictive control improvements, and optimizations through virtual and physical entities exchange. This paper has developed two generalized dynamic models, one using ANFIS systems and another using phenomenological modeling using Partial Differential Equations (PDE) and parameter identification tools. The models describe the FSC outlet temperature day and night during plant start-up, operation, and shut-down. The total available data consists of 25 days of measurement data with a sampling time of $t_s = 20$ s, resulting in 101 854 total samples. The twinning process for the ANFIS is its training and checking, while for the PDE model is the identification procedure. The PDE model identification procedure has a higher computational burden than the ANFIS. Thus, it was necessary to reduce the PDE model twinning input data, resulting in four days for identification, while the ANFIS model utilizes 19 days for training and checking. The developed models have shown the following features:

1. The models are validated and have defined accuracy and precision indexes accordingly to error mean, standard deviation, standard error, and mean absolute percentage error considering six days of operation data and 23 822 samples.
2. All models follow actual measurement trends during the day and night with a worst-case mean error of 0.51 °C, a worst-case standard deviation of 5.09 °C (95% confidence interval), and a worst-case mean absolute percentage error of 2.49%
3. The models consider the primary mirrors variable focus as model inputs; therefore, this work states and validate the first FSC dynamic model with the focus/defocus effect on the outlet temperature.
4. PDE model and NF model with integration steps of 5 s run one day of operation in 340.28 s and 59.14 s, with a simulation time step of 19.7 ms and 3.4 ms, respectively; therefore, fast enough to be used in Model Predictive Control (MPC) techniques.
5. The NF model with integration steps of 20 s runs one day of operation in 5.79 s and one simulation step in 1.3 ms. Therefore, almost three times faster than the NF with dt = 5 s and more than fifteen times faster than the PDE.
6. The models run a twinning, coping with plant aging or process modifications because the neuro-fuzzy ANFIS is an adaptive technique, and the identification procedure can update the PDE model parameters.
7. The PDE model takes 785.01 min twinning one day of operation data, while the NF model takes 22.53 min, considering $t_s = 5$ s. The NF model twinning with $t_s = 20$ s takes 7.71 min. Thus, the ETSI solar absorption plant twinning can occur at night or on the weekend when the plant is off.

In conclusion, this work contributes to the dynamic modeling of an FSC, considering its further use as a digital entity on a digital twin framework. Future works will further model the long pipes that connect the absorption chiller and the FSC to consolidate the whole plant's digital twin. Furthermore, the plant DT will unlock control and optimization investigations, offering several possibilities for the operation of the plant enhancements and scientific contributions.

CRediT authorship contribution statement

Diogo Ortiz Machado: Conceptualization, Methodology, Software, Validation, Formal analysis, Investigation, Visualization, Writing – original draft. **William D. Chicaiza:** Methodology, Software, Investigation, Visualization, Writing – original draft. **Juan M. Escaño:** Resources, Writing – review & editing, Supervision, Project administration. **Antonio J. Gallego:** Data curation, Writing – review & editing. **Gustavo A. de Andrade:** Software, Writing – review & editing, Supervision. **Julio E. Normey-Rico:** Writing – review & editing, Supervision, Funding acquisition. **Carlos Bordons:** Writing – review & editing, Supervision, Project administration, Funding acquisition . **Eduardo F. Camacho:** Resources, Data curation, Project administration, Funding acquisition.

Declaration of competing interest

The authors declare the following financial interests/personal relationships which may be considered as potential competing interests: Diogo Ortiz Machado reports financial support was provided by Federal Institute of Education Science and Technology of Rio Grande do Sul. William David Chicaiza reports financial support was provided

by University of Seville. Juan Manuel Escano reports financial support was provided by University of Seville. Antonio Gallego reports financial support was provided by University of Seville. Gustavo A. de Andrade reports financial support was provided by Federal University of Santa Catarina. Julio Elias Normey-Rico reports financial support was provided by Federal University of Santa Catarina. Carlos Bordons reports financial support and article publishing charges were provided by University of Seville. Eduardo F. Camacho reports financial support was provided by University of Seville.

Data availability

I have shared my data/code in MendeleyData. The link is https://data.mendeley.com/datasets/rzggrvczf6 which is also in the Article's Appendix.

Acknowledgments

The authors would like to acknowledge the Coordenação de Aperfeiçoamento de Pessoal de Nível Superior (CAPES), Brazil, Finance Code 001, the Conselho Nacional de Desenvolvimento Científico e Tecnológico (CNPq), Brazil, under grant 304032/2019–0. The Agencia Estatal de Investigación (AEI) of the Spanish Ministry of Science and Innovation, under grant PID2019-104149RB-I00/10.13039/501100011033 (project SAFEMPC), to the European Commission for funding this work under Project DENiM. This project has received funding from the European Union's Horizon 2020 research and innovation programme under grant agreement No 958339 and the European Research Council under Advanced Research Grant OCONTSOLAR (789051). Diogo O. Machado thanks to *Fundación Carolina*, SEGIB, and PrInt-UFSC programs for mobility scholarships. This study was supported by the Federal Institute of Education, Science and Technology of Rio Grande do Sul (IFRS), Brazil.

Appendix. Validation data

Supplementary data associated with the validation of this article can be found in https://data.mendeley.com/datasets/rzggrvczf6/1 [54].

References

[1] United Nations. United nations framework convention on climate change united nations. U N Frameork Conv Clim Change 1992;1–33, URL https://treaties.un.org/pages/ViewDetailsIII.aspx?src=TREATY&mtdsg_no=XXVII-7&chapter=27&Temp=mtdsg3&clang=_en.

[2] United Nations Organization. 7Th sustainable development goal. 2019, URL https://www.un.org/sustainabledevelopment/energy/.

[3] International Energy Agency. Net zero by 2050 - A roadmap for the global energy sector. IEA 2021. URL https://www.iea.org/reports/net-zero-by-2050.

[4] Lindmark S. The role of absorption cooling for reaching sustainable energy systems. (Master's thesis), Stockolm: KTH; 2005.

[5] Esfanjani P, Jahangiri S, Heidarian A, Valipour MS, Rashidi S. A review on solar-powered cooling systems coupled with parabolic dish collector and linear Fresnel reflector. Environ Sci Pollut Res 2022;29:42616–46. http://dx.doi.org/10.1007/S11356-022-19993-3/FIGURES/9, URL https://link.springer.com/article/10.1007/s11356-022-19993-3.

[6] Moran M, Shapiro H, Boettner D, Bailey M. Fundamentals of engineering thermodynamics. 8th ed.. Wiley; 2014, URL https://books.google.com.br/books?id=uxObAwAAQBAJ.

[7] Jie S, Zhang Z, Wang L, Zhenwen Z, Jinjia W. Comprehensive review of line-focus concentrating solar thermal technologies: Parabolic trough collector (PTC) vs linear Fresnel reflector (LFR). J Therm Science 2020;29. http://dx.doi.org/10.1007/s11630-020-1365-4.

[8] Ahmad MW, Mourshed M, Yuce B, Rezgui Y. Computational intelligence techniques for HVAC systems: A review Article History. Build Simul 2016. http://dx.doi.org/10.1007/s12273-016-0285-4.

[9] Mondejar ME, Avtar R, Diaz HLB, Dubey RK, Esteban J, Gómez-Morales A, Hallam B, Mbungu NT, Okolo CC, Prasad KA, She Q, Garcia-Segura S. Digitalization to achieve sustainable development goals: Steps towards a smart Green Planet. Sci Total Environ 2021;794:148539. http://dx.doi.org/10.1016/J.SCITOTENV.2021.148539.

[10] Skogestad S. Plantwide control: the search for the self-optimizing control structure. J Process Control 2000;10:487–507. http://dx.doi.org/10.1016/S0959-1524(00)00023-8.

[11] Chachuat B, Srinivasan B, Bonvin D. Adaptation strategies for real-time optimization. Comput Chem Eng 2009;33(10):1557–67. http://dx.doi.org/10.1016/j.compchemeng.2009.04.014, URL https://www.sciencedirect.com/science/article/pii/S0098135409001082, Selected Papers from the 18th European Symposium on Computer Aided Process Engineering (ESCAPE-18).

[12] Camacho E, Bordons C. Model predictive control. Springer-Verlag London; 2007, http://dx.doi.org/10.1007/978-0-85729-398-5.

[13] Machado DO, Andrade GA, Normey-Rico JE, Bordons C. Optimal operation of Concentrating Solar Collector fields using exergy-based hierarchical control. Energy 2022;239:122462. http://dx.doi.org/10.1016/J.ENERGY.2021.122462.

[14] Sánchez AJ, Gallego AJ, Escaño JM, Camacho EF. Hierarchical set-point optimization and feedforward strategy for collector defocusing of a solar plant. Sol Energy 2021;220:282–94. http://dx.doi.org/10.1016/j.solener.2021.01.019.

[15] Berenguel M, Cirre CM, Klempous R, Maciejewski H, Nikodem M, Nikodem J, Rudas I, Valenzuela L. Hierarchical control of a distributed solar collector field. In: Lecture notes in computer science (including subseries lecture notes in artificial intelligence and lecture notes in bioinformatics). LNCS, Vol. 3643, 2005, p. 614–20. http://dx.doi.org/10.1007/11556985_82.

[16] Yip W, Marlin T. The effect of model fidelity on real-time optimization performance. Comput Chem Eng 2004;28(1):267–80. http://dx.doi.org/10.1016/S0098-1354(03)00164-9, URL https://www.sciencedirect.com/science/article/pii/S0098135403001649, Escape 12.

[17] Picard D, Drgoa J, Kvasnica M, Helsen L. Impact of the controller model complexity on model predictive control performance for buildings. Energy Build 2017;152:739–51. http://dx.doi.org/10.1016/j.enbuild.2017.07.027, URL https://www.sciencedirect.com/science/article/pii/S0378778817302190.

[18] Biegler L, Yang X, Fischer G. Advances in sensitivity-based nonlinear model predictive control and dynamic real-time optimization. J Process Control 2015;30:104–16. http://dx.doi.org/10.1016/j.jprocont.2015.02.001, URL https://www.sciencedirect.com/science/article/pii/S0959152415000281, CAB/DYCOPS 2013.

[19] Ellis M, Durand H, Christofides PD. A tutorial review of economic model predictive control methods. J Process Control 2014;24(8):1156–78. http://dx.doi.org/10.1016/j.jprocont.2014.03.010, URL https://www.sciencedirect.com/science/article/pii/S0959152414000900, Economic nonlinear model predictive control.

[20] Zanin A, Tvrzská de Gouvêa M, Odloak D. Integrating real-time optimization into the model predictive controller of the FCC system. Control Eng Pract 2002;10(8):819–31. http://dx.doi.org/10.1016/S0967-0661(02)00033-3, URL https://www.sciencedirect.com/science/article/pii/S0967066102000333.

[21] Rasheed A, San O, Kvamsdal T. Digital twin: Values, challenges and enablers from a modeling perspective. IEEE Access 2020;8:21980–2012. http://dx.doi.org/10.1109/ACCESS.2020.2970143.

[22] Liu M, Fang S, Dong H, Xu C. Review of digital twin about concepts, technologies, and industrial applications. J Manuf Syst 2021;58:346–61. http://dx.doi.org/10.1016/j.jmsy.2020.06.017, URL https://www.sciencedirect.com/science/article/pii/S0278612520301072, special issue: Digital Twin towards Smart Manufacturing and Industry 4.0.

[23] Tao F, Zhang H, Liu A, Nee AY. Digital twin in industry: State-of-the-art. IEEE Trans Ind Inf 2019;15:2405–15. http://dx.doi.org/10.1109/TII.2018.2873186.

[24] Bermejo P, Pino FJ, Rosa F. Solar absorption cooling plant in Seville. Sol Energy 2010;84:1503–12. http://dx.doi.org/10.1016/j.solener.2010.05.012.

[25] Ceusters G, Rodríguez RC, García AB, Franke R, Deconinck G, Helsen L, Nowé A, Messagie M, Camargo LR. Model-predictive control and reinforcement learning in multi-energy system case studies. Appl Energy 2021;303:117634. http://dx.doi.org/10.1016/j.apenergy.2021.117634, URL https://www.sciencedirect.com/science/article/pii/S0306261921010011.

[26] Ghilardi LMP, Castelli AF, Moretti L, Morini M, Martelli E. Co-optimization of multi-energy system operation, district heating/cooling network and thermal comfort management for buildings. Appl Energy 2021;302:117480. http://dx.doi.org/10.1016/j.apenergy.2021.117480, URL https://www.sciencedirect.com/science/article/pii/S0306261921008680.

[27] Pino F, Caro R, Rosa F, Guerra J. Experimental validation of an optical and thermal model of a linear fresnel collector system. Appl Therm Eng 2013;50(2):1463–71. http://dx.doi.org/10.1016/j.applthermaleng.2011.12.020, URL https://www.sciencedirect.com/science/article/pii/S1359431111007174, Combined Special Issues: ECP 2011 and IMPRES 2010.

[28] Machado DO, Sánchez AJ, Gallego AJ, de Andrade GA, Normey-Rico JE, Bordons C, Camacho EF. Split-range control for improved operation of solar absorption cooling plants. Renew Energy 2022;192:361–72. http://dx.doi.org/10.1016/j.renene.2022.04.064, URL https://www.sciencedirect.com/science/article/pii/S0960148122005249.

[29] Jones D, Snider C, Nassehi A, Yon J, Hicks B. Characterising the digital twin: A systematic literature review. CIRP J Manuf Sci Technol 2020;29:36–52. http://dx.doi.org/10.1016/J.CIRPJ.2020.02.002.

[30] Tao F, Qi Q, Wang L, Nee AY. Digital twins and cyber–physical systems toward smart manufacturing and industry 4.0: Correlation and comparison. Engineering 2019. http://dx.doi.org/10.1016/j.eng.2019.01.014.

[31] Granacher J, Nguyen T-V, Castro-Amoedo R, Maréchal F. Overcoming decision paralysis—A digital twin for decision making in energy system design. Appl Energy 2022;306:117954. http://dx.doi.org/10.1016/j.apenergy.2021.117954, URL https://www.sciencedirect.com/science/article/pii/S0306261921012629.

[32] Robledo M, Escaño JM, nez AN, Bordons C, Camacho EF. Development and experimental validation of a dynamic model for a fresnel solar collector. IFAC Proc Vol 2011;44. http://dx.doi.org/10.2514/6.2015-1563, URL https://www.sciencedirect.com/journal/ifac-proceedings-volumes/vol/44/issue/1.

[33] Spoladore M, Camacho EF, Valcher ME. Distributed parameters dynamic model of a solar fresnel collector field. In: IFAC proceedings volumes (IFAC-papersonline), Vol. 44. IFAC Secretariat; 2011, p. 14784–9. http://dx.doi.org/10.3182/20110828-6-IT-1002.02992.

[34] Chicaiza WD, Sánchez AJ, Gallego AJ, Escaño JM. Neuro-fuzzy modelling of a linear fresnel-type solar collector system as a digital twin. In: Joint proceedings of the 19th world congress of the international fuzzy systems association (IFSA), the 12th conference of the european society for fuzzy logic and technology (EUSFLAT), and the 11th international summer school on aggregation operators (AGOP). Atlantis Press; 2021, p. 242–9. http://dx.doi.org/10.2991/asum.k.210827.033.

[35] Jang J-S. ANFIS: adaptive-network-based fuzzy inference system. IEEE Trans Syst Man Cybern 1993;23(3):665–85. http://dx.doi.org/10.1109/21.256541.

[36] Camacho E, Berenguel M, Rubio FR, Martínez D. Control of solar energy systems. Springer London Dordrecht Heidelberg New York; 2006, http://dx.doi.org/10.1007/978-0-85729-916-1.

[37] Industrial Solar. Fresnel Collector LF-11 datasheet. 2007, URL https://www.google.com/search?q=Industrial+solar+LF-11&source=lmns&bih=625&biw=1366&hl=pt-BR&ved=2ahUKEwibir29u8DoAhUzCbkGHetXBnwQ_AUoAHoECAEQAA.

[38] Schott Solar. SCHOTT PTR70 receiver the 4 th generation. 2013, URL https://d3pcsg2wjq9izr.cloudfront.net/files/31497/download/461508/1-schott_ptr70_4th_generation_brochure.pdf.

[39] Brownlee J. Data preparation for machine learning data cleaning, feature selection, and data transforms in python. Jason Brownlee; 2020, URL http://14.99.188.242:8080/jspui/handle/123456789/16327?mode=full.

[40] Wang RY, Strong DM. Beyond accuracy: What data quality means to data consumers. J Manage Inf Syst 1996;12(4):5–33. http://dx.doi.org/10.1080/07421222.1996.11518099, arXiv:https://doi.org/10.1080/07421222.1996.11518099.

[41] Pyle D. Data preparation for data mining. Morgan Kaufmann Publishers; 1999.

[42] Batini C, Milano PD, Maurino A. Methodologies for data quality assessment and improvement CINZIA CAPPIELLO CHIARA FRANCALANCI. ACM Comput Surv 2009;41:16. http://dx.doi.org/10.1145/1541880.1541883.

[43] Brandão ASM, da Costa Mendes PR, Normey-Rico JE. Simplified optical model, aiming strategy and partial defocusing strategy for solar Fresnel collectors. Renew Energy 2022;188:11–36. http://dx.doi.org/10.1016/J.RENENE.2022.02.019.

[44] Normey-Rico JE, Bordons C, Berenguel M, Camacho EF. A robust adaptive dead-time compensator with application to a solar collector Field1. IFAC Proc Vol 1998;31(19):93–8. http://dx.doi.org/10.1016/S1474-6670(17)41134-7, URL https://www.sciencedirect.com/science/article/pii/S1474667017411347, IFAC Workshop on Linear Time Delay Systems (LTDS '98), Grenoble, France, 6-7 July.

[45] Kincaid N, Mungas G, Kramer N, Wagner M, Zhu G. An optical performance comparison of three concentrating solar power collector designs in linear Fresnel, parabolic trough, and central receiver. Appl Energy 2018;231:1109–21. http://dx.doi.org/10.1016/j.apenergy.2018.09.153, URL https://www.sciencedirect.com/science/article/pii/S0306261918314648.

[46] Shampine LF, Reichelt MW, Comput SJS. THE MATLAB ODE SUITE *. Soc Ind Appl Math 1997;18:1–22, URL http://www.siam.org/journals/sisc/18-1/27642.html.

[47] Byrd RH, Gilbert JC, Nocedal J. A trust region method based on interior point techniques for nonlinear programming. Math Program Ser B 2000;89:149–85. http://dx.doi.org/10.1007/PL00011391.

[48] Zadeh L. Fuzzy sets. Inf Control 1965;8(3):338–53. http://dx.doi.org/10.1016/S0019-9958(65)90241-X.

[49] Zadeh LA. Outline of a new approach to the analysis of complex systems and decision processes. IEEE Trans Syst Man Cybern 1973;SMC-3(1):28–44. http://dx.doi.org/10.1109/TSMC.1973.5408575.

[50] Jang J, Sun C, Mizutani E. Neuro-fuzzy and soft computing: a computational approach to learning and machine intelligence. MATLAB curriculum series, Prentice Hall; 1997, URL https://books.google.com.br/books?id=vN5QAAAAMAAJ.

[51] Takagi T, Sugeno M. Derivation of fuzzy control rules from human operator's control actions. IFAC Proc Vol 1983;16(13):55–60. http://dx.doi.org/10.1016/S1474-6670(17)62005-6, IFAC Symposium on Fuzzy Information, Knowledge Representation and Decision Analysis, Marseille, France, 19-21 July, 1983.

[52] Chiu SL. Fuzzy model identification based on cluster estimation. J Intell Fuzzy Systems 1994;2(3):267–78.

[53] Werbos PJ. Beyond regression : new tools for prediction and analysis in the behavioral sciences (Ph.D. thesis), Cambridge, Massachusetts: Harvard University; 1974.

[54] Machado D, Chicaiza W, Escaño JM, Gallego A, de Andrade G, Normey-Rico J, Bordons C, Camacho E. Digital twin of a Fresnel solar collector for solar cooling - validation data. Mendeley Data 2022;1. http://dx.doi.org/10.17632/RZGGRVCZF6.1.